Molecular structure, spectroscopy, quantum chemical and antibacterial activity investigations of 2-methylbenzylammonium perchlorate

C. Daghar, N. Issaoui, H. Marouani, T. Roisnel, O. Al-Dossary

Molecular structure, spectroscopy, quantum chemical and antibacterial activity investigations of 2-methylbenzylammonium perchlorate

Chaima Daghar[a], Noureddine Issaoui[b], Houda Marouani[a], Thierry Roisnel[c]

[a]Université de Carthage, Faculté des Sciences de Bizerte, LR13ES08 Laboratoire de Chimie des Matériaux, 7021, Bizerte,Tunisie
[b]University of Monastir, Laboratory of Quantum and Statistical Physics LR18ES18, Faculty of Sciences, Monastir 5079, Tunisia
[c]Univ Rennes, CNRS, ISCR (Institut des Sciences Chimiques de Rennes) – UMR 6226, F-35000 Rennes, France

*Correspondence e-mail: houdamarouani2015@gmail.com

Abstract

A new organic inorganic hybrid $(C_8H_{12}N)ClO_4$ has been synthesized and characterized by spectroscopic (FT-IR,^{13}C NMR and UV-Visible) and single crystal X-ray studies. These properties of 2-methylbenzylammonium perchlorate were also evaluated by DFT method.
The title compound crystallized in the monoclinic space group $P2_1/c$ at room temperature by slow evaporation with the following parameters a = 6.8894 (5) Å, b = 4.9146 (4) Å, c = 29.6565 (18) Å, β = 96.006°, Z = 4 and V= 998.62(12) Å^3. The crystal packing is determined by N–H…O, C–H…O hydrogen bonds and C–H…π interactions. The intermolecular interactions in the crystal structure were quantified and analyzed using Hirshfeld surface analysis. In addition the vibrational assignments, chemical shifts and geometrical parameters (bond lengths, bond angles, torsion angles) of the compound were calculated and found in good agreement with experimental results as well as the ^{13}C NMR spectra are in agreement with the X-ray structure. Furthermore, the optical properties of the synthesized compound were investigated by UV-Vis and luminescence spectroscopy. Molecular electronic potential (MEP) has been calculated by the DFT calculation method. Reduced density gradient (RDG) and atoms in molecules (AIM) studies have also been performed to investigate the nature and strength of hydrogen bonding interactions. Also the HOMO and LUMO analysis have been used to confirm the experimental energy band gap of the compound. Finally, the biological activities of the new compound against four bacteria are also tested showing promising antimicrobial activity.

Keywords: Hybrid material; XRD; NMR; DFT calculations; Hirshfeld surface; antimicrobial activity.

1. Introduction

In the last decades organic-inorganic hybrid compounds has attracted considerable and remarkable attention in solid state chemistry due to their ability to combine both the properties of inorganic compounds such as electronic properties and organic molecules such as flexibility, luminescence and photosensitivity. This symbiosis between two types of chemistry for too long considers being as antagonists gives birth to completely new properties and opens up a vast field of investigation for the chemist. In this context, these hybrid materials are used in a wide range of applications such as biology [1,2], medicine [3,4], optics, electrical conductivity, photochemistry [5,6] and photo catalysis [7]. Moreover hybrid compounds play an important role in cell metabolism; they are involved in energy transfer due to their richness in intermolecular interactions via hydrogen bridges.

In particular hybrid compounds based on perchlorates have brought current interest because of its chemical properties and their physical nature. They are characterized by their extreme solubility and poor adsorption [8]. Perchlorates (ClO_4^-) occur naturally in nitrate deposits and potash ore. It can also be present in air, soil and water. It has also been detected in a variety of food products such as milk [9], lettuce and wheat [10,11]. Furthermore Environmental perchlorate exposure is of potential health concern since it can work by disrupting the function of the thyroid gland, or by hindering the absorption of iodine, high doses of perchlorate have been used to treat hyperthyroidism in humans [12-14].

The present work was attempted the new hybrid compound 2-methylbenzylammonium perchlorate with formula $(C_8H_{12}N)ClO_4$. The new material has been characterized by X-ray diffraction to determine the crystallographic characteristics and atomic arrangements. Besides, Hirshfeld surface analysis and the associated contacts enrichment ratio (ER) were investigated to evaluate the contributions of different intermolecular interactions. It also makes use of the infrared spectroscopy to identify the different vibrational assignments present in the compound. The UV-visible was used for investigation of electronic transitions, and the optical band gaps for the title compound.

The theoretical investigation was performed and compared to the experimental results. The molecular electrostatic potential (MEP), frontier orbitals (HOMO-LUMO), topological properties AIM and RDG were obtained computationally.

2. Experimental details

2.1. Synthesis and crystallization

Stoichiometric solution of perchloric acid (0.1 g, 1 mmol, purity 70%, Aldrich) is added drop wise to a solution of 2-methylbenzylamine (0.1 g, 1 mmol, purity 96%, Aldrich) dissolved in ethanol. The mixture is left under stirring at room temperature for 30 minutes. Two weeks later single crystals of $(C_8H_{12}N)ClO_4$ are formed into fine colorless needles. The crystals can be stable for month under normal conditions of temperature and humidity. Schematically the reaction can be written as follow:

$$C_8H_{11}N + HClO_4 \xrightarrow{EtOH\ /H_2O} (C_8H_{12}N)ClO_4$$

Elemental analysis, calc. (found): C, 43.43% (43.32); H, 5.41% (5.38) ; N, 6.32% (6.35).

2.2. X-ray data collection and physical measurements

Diffraction data of the title compound was collected at 150K with D8 VENTURE Bruker AXS diffractometer equipped with graphite monochromatic MoKα radiation (λ= 0.71073Å). Absorption corrections were performed using the multi-scan technique using the SADABS program [15]. The total number of measured reflections was 7298 among which 2282 were independent and 1948 had the intensity $I > 2\sigma(I)$. The structure was solved by direct methods using SHELXT program, which revealed the position of all non-hydrogen atoms, and then refined with full-matrix least-square methods based on F^2 (SHELXL) [16] included in the WINGX program [17]. A final refinement on F^2 converged at $R(F^2) = 0.061$ and $wR(F^2) = 0.152$. The crystallographic data and the structure refinements are summarized in **Table 1**. An ORTEP drawing of the molecular arrangement is shown in Fig. 1a.

The experimental IR spectrum was obtained on Perkin-Elmer FT-IR 1000 spectrometer equipped with a diamond micro-ATR access at room temperature in the frequency range 4000-400 cm^{-1}. Solid state UV-Vis spectrum was performed on a Perkin Elmer Lambda35 spectrophotometer from the range of 200–800 nm. Fluorescent spectra were recorded for the solid sample at room temperature with Perkin-Elmer LS55 spectrofluorometer.

2.3. Computational details

In this theoretical study, all the calculations were performed using the GaussView program [18] and the Gaussian 09 software package [19] by using the Density functional theory (DFT) with the Becke-three-parameter hybrid exchange functional combined with the Lee-Yang-Parr correlation functional (B3LYP) [20,21] levels, the 6-311++G(d,p) basis set was used for all.

In order to analyze the intramolecular interactions, Hirshfeld surfaces and their associated two-dimensional fingerprint plots were performed by the Crystal Explorer version 3.1 software [22] program imported on a CIF file. The topological properties were calculated by the Multiwfn program package [23] as well as the reduced density gradient are graphed by Multiwfn and plotted by the VMD program [24]. Frontier molecular orbitals (HOMO, LUMO), band gap and molecular electrostatic potential (MEP) were also computed.

2.4. Antibacterial activity determination

The antimicrobial activity of the title compound against four different pathogenic organisms, two pathogenic gram-negative strains such as *Escherichia coli* ATCC 8739 G(-) and *Salmonella typhimurium* ATCC 14028 G(-) gram and two pathogenic gram-positive strains such as *Staphylococus aureus* ATCC 6538 G(+) and *Enterococcus feacium* ATCC 19434 G(+) by the modified agar diffusion method [25-27].

A suspension of the tested microorganisms was spread on the appropriate solid media plates and incubated overnight at 37°C. After 1 day, 4-5 loops of pure colonies were transferred to saline solution in a test tube for each bacterial strain and adjusted to the 0.5 McFarland turbidity standards (~10^8 cells/mL). Sterile cotton dipped into the bacterial suspension and the agar plates were streaked three times, each time turning the plate at a 60° angle and finally rubbing the swab through the edge of the plate. Sterile paper discs (Glass Microfibre filters, Whatman; 6 mm in diameter) were placed onto inoculated plates and impregnated with the diluted solutions in sterile water. Ampicillin (10µg/disc) was used as positive control for all strains except *Candida albicans* for which Nystatin (100µg/disc) was used. Inoculated plates with discs were placed in a 37°C incubator. After 24 hours of incubation, the results were recorded by measuring the zones of growth inhibition surrounding the disc. Clear inhibition zones around the discs indicated the presence of antimicrobial activity. The test was run in duplicate.

The antifungal activity of this compound and the reacting agents were tested against the fungi, *Candida albicans* ATCC 10231. Nystatin was used as standard fungicide and DMSO served as a resource of control.

3. Results and discussion

3.1. X-ray diffraction and geometry optimization

2-methylbenzylammonium perchlorate crystallizes in centrosymmetric monoclinic system, space group $P2_1/c$ (**Table 1**). The crystal has four formula units per unit cell with the lattice constants a = 6.8894 (5) Å, b = 4.9146 (4) Å, c = 29.6565 (18) Å and β = 96.006(2)°. The Ortep representation and the optimized geometric model of $(C_8H_{12}N)ClO_4$ are shown in Figs.1a,b.

The asymmetric unit is comprised of one cationic entity ($C_8H_9NH_3^+$) and one anionic entity (ClO_4^-) (Fig. 1a). The cohesion between ($C_8H_9NH_3^+$) cations and (ClO_4^-) anions is ensured by C-H...O and N-H…O hydrogen bonds to form a three-dimensional network (Fig. 2a).

The projection of the atomic arrangement of the title compound along the [100] direction displayed in Fig. 2b clearly shows that the perchlorate ClO_4 entities are located in position z=0 and z=1/2 between which the organic cations are inserted in zigzag along c in position z=1/4 and z=3/4.

The bond lengths and the bond angles obtained from the X-ray crystallographic data are compared with computational results by B3LYP/6-311++G(d,p) method, as shown in **Table 2**.

The perchlorate anion is composed of a chlorine atom bonded to four oxygen atoms giving rise to distorted tetrahedron. The Cl-O distances bonds vary from 1.411(3) Å to 1.430(2) Å for XRD and 1.468 Å to 1.532 Å for DFT. The O-Cl-O bond angles range from 108° (17) to 110.7°(2) for XRD and 106.07° to 112.54° for DFT which confirms the distortion of the tetrahedron. These bond lengths and angles (**Table 2**) are in good agreement with those observed in similar compounds based on perchlorate [28,29]. In this structure, the average values of the distortion parameters of the ClO_4 are calculated by using Baur method [30]. The values of the distortion indices were DI (ClO) = 0.004; DI (OO) = 0.0055 and DI (OClO) = 0.0093, show a strong distortion of OClO angles compared to O-O and ClO distances. It can

be assumed that ClO_4 tetrahedra are formed by a regular arrangement of oxygen atoms, with chlorine atom is slightly displaced from the center of gravity of the tetrahedron.

Concerning the organic cation, the protonation on the N site is confirmed from the elongated C-N bond distance it is equal to d_{N-C} = 1,472(4) Å (1,509 Å: calculated) (**Table 2**) and the angles values of N-C-C are 112,5°(2) (111,4°: calculated). The C-C bond lengths in the phenyl ring varying from 1.372(5) Å to 1.406(4) Å with an average values 1.389 Å for the observed XRD values and 1.3911 Å to 1.409 Å for the calculated values. The C-C-C angles extend from 119.1° (3) to 122.3° (3). These results are similar to those observed in other compounds with similar amine [31,32].

The aromatic ring of the cation is essentially planar with an r.m.s deviation (root mean square) of 0.0029Å. These values show clearly that the carbon ring in the phenyl groups is regular.

The organic cations are approximately parallel and equidistant from each other as shown in Fig.2c. Besides, the shortest distances between the centroids of the rings is 4.915 Å excluding the presence of π–π stacking interactions.

We notice that the optimized values and experimental bond length and angle are slightly different. This difference is due to that the experimental data was obtained in the solid state while theoretical calculations were performed in the gas phase without considering lattice interactions. On average the observed and calculated parameters were approximately in good agreement with the experimental one.

The hydrogen bonds play an important role in stabilizing the crystal packing in particular the hydrogen atoms bonded to the 2-methylbenzylammonium contribute to the formation of N-H…O and C-H…O hydrogen bonding pattern with perchlorate anions where N-H…O with donor-acceptor distances varying between 2.861 (3) Å and 2.927 (5) Å and C-H…O range from 3.459 (4) Å to 3.549 (4) Å (**Table 3**). Organic cations are also connected together via C…H-$\boldsymbol{\pi}$ interactions forming subsequently thick infinite sheets situated around z=1/4 and ¾ (Fig. 2b) with donor-acceptor distances 3.997Å and 4.120 Å. Indeed inside this arrangement (Fig. 2c), the entities are interconnected via multiple hydrogen bonds generate rings forming $R_4^4(12)$ and $R_1^2(5)$ motifs.

3.2. Hirshfeld surface analysis

The Hirshfeld surface analysis was carried out in order to examine the intermolecular interactions present in the crystal structures. Using the CIF files Crystal-Explorer 3.1 [22] can compute the Hirshfeld surface and then the fingerprint plots.

The Hirshfeld surface of the title compound is displayed in Fig. 3, showing surface that have been mapped over a d_{norm}, Shape index and curvedness properties of the $(C_8H_{12}N)ClO_4$ compound. The representation in $\mathbf{d_{norm}}$ shows a surface with a color scheme where the bright red region illustrates shorter contacts ($d_{norm} < 0$) and indicate the existence of N-H ...O and C-H …O hydrogen bonding. The blue spots illustrate the longest contacts in the structure ($d_{norm} > 0$) and the white spots is used for the contacts around the sum of van der Waals separation ($d_{norm} = 0$). The shape index cartography shows that there are no adjacent red and blue triangles and the small flat segments delineated by blue contours on the curvedness mapping exclude the presence of π–π interactions in our crystal structure.

The overall two dimensional fingerprint plot and the two-dimensional fingerprint plots are used to analyze the contribution of every intermolecular interaction in crystal structure stabilization and illustrated in Fig. 4. The examination of these plots show that the major part of the surface of Hirshfeld is occupied by the contacts O ⋯ H / H ⋯ O (44%) which are attributed to the hydrogen bonds of type C-H… O and N-H… O. They are characterized by two pointed and symmetrical points with a sum of ($d_e + d_i \sim 1.85$Å) which is less than the sum of the van der Waals radii (H: 1.09Å, O: 1.52 Å) which confirms that these intermolecular contacts are considered as close contacts.

H… H contacts comprise 34.1% of the total Hirshfeld Surface and appear with high concentration in the middle of the fingerprint patch. C… H / H… C contacts are represented by a pair of symmetrical wings and cover 14.6% of the entire Hirshfeld surface with a sum of ($d_e + d_i \sim 2.8$Å) smaller than the sum of the van der Waals radii of the carbon (3.4 Å) and hydrogen (1,09Å) atoms, it confirms that the inter-contact is considered as being close contact. These data are characteristic of a C-H…π interaction. Finally the C… O/O…C (0.2%), C… C (0.7%) and O… O (6.3%) contacts have very low contribution to the Hirshfeld surface and they are negligible.

We have also determined the enrichment ratios (ER) of the intermolecular contacts for the molecule. The enrichment ratio ER_{XY} of a pair of chemical elements (X,Y) are obtained from the actual contacts between the different chemical species (X,Y) and the theoretical proportion of random contacts [33]. The ER values are summarized in **Table 4**. The H…O/O…H appear with an enrichment ratios ($ER_{OH} = 1.22$) are favored in the crystal package with the formation of the hydrogen bonds N-H ... O and C-H ... O type. The H…H contacts appear with an enrichment ratios close to unity ($ER_{HH} = 0.85$) this value is in good agreement with the expectation of Jelch. The strong enrichment of C…H/H…C contact (ER_{CH}

= 1.42) confirm the presence of C-H…π stacking, this is confirmed by single crystal structure investigation.

We conclude that the Hirshfeld surface analysis confirms the importance of hydrogen bonding in establishing the packing.

3.3. Vibrational spectral analysis

In order to give more information about the crystal structure, infrared spectroscopy has been used to identify the functional groups present in the crystal and to investigate their vibrational behavior in the solid state.

The infrared spectrum was recorded at room temperature in the 4000-400 cm^{-1} range and compared to the theoretical spectrum by using the density functional theory (DFT) method associated with the B3LYP/6-311 ++ G (d,p) basis set on the optimized geometries of the title compound. The calculated and experimental infrared spectra are shown in Fig. 5. The vibrational spectra showed good correlations with the experimental data with slight difference between the experimental and the theoretical spectra. These small differences which may be due to the fact that the DFT calculations were carried in the gas phase where the crystalline packing forces were not considered.

Vibrations of perchlorate anion

Based essentially on comparison with previous works reported on perchlorate compounds experimental spectra and theoretical calculations, a tentative assignment of the observed bands may be proposed [28]. The bands at 854 and 1056 cm^{-1} are assigned to the symmetric and asymmetric stretching mode of ClO_4^- units. The computations data give the frequency of these bands at 862 cm^{-1} for the symmetric stretching and 1082 cm^{-1} for the asymmetric stretching vibrations ν_s (ClO_4^-).

The bands appearing at 448 and 623 cm^{-1} correspond to the symmetric and asymmetric bending mode of ClO_4^-. The DFT calculation gives these modes at 443 and 573 cm^{-1}.

Vibrations of organic cation

The high wavenumbers observed between 3498 and 3138 cm^{-1} is assigned to the N-H asymmetric and symmetric stretching vibration. In the theoretical FT IR spectrum, these bands are observed between 3517 and 3148 cm^{-1}.

The absorption bands appeared at 3267–3138 cm^{-1} indicated the presence of aromatic C–H stretching vibrations and which corresponds to a theoretical value 3168-3118 cm^{-1}.

The frequencies between 1609 and 1480 cm^{-1} are assigned to the asymmetric and symmetric stretching vibrations of NH_3^+ and C=C stretching vibration of the aromatic ring. The calculated peaks are located at 1641 and 1412 cm^{-1}.

The absorption at 3046 and 2936 cm^{-1} are due to the asymmetric and symmetric stretching of ($-CH_2$). The DFT computations give the frequency of these bands at 3048 and 3008 cm^{-1}. Also the bands in the wavenumber region 1111-1019 cm^{-1} are associated to C-H in-plane and out of plane bending vibration, C-N stretching vibration and asymmetric and symmetric C-C stretching modes. These modes are computed at1092-1002 cm^{-1}.

3.4. NMR chemical shifts

The ^{13}C NMR experimental spectrum of 2-methylbenzylammonium perchlorate crystals is shown in Fig. 6. ^{13}C NMR chemical shifts computed at B3LYP/6-311 + G (2d,p) level of theories with GIAO approach [34] have been compared with the experimental data and summarized in **Table 5**. The method theoretical employed equally give reasonable agreement with the experimental values.

The peak at 20 ppm is due to aliphatic carbon methyl group (C9) whereas the computed chemical shift value is 29.386 ppm. The multiplet peaks observed between δ = 39.14 ppm and δ = 39.98 ppm have been assigned to the DMSO solvent. The singlet at δ = 38.97 ppm (29.386 ppm calculated) is assigned to the carbone (C2) attached to the NH_3 amino group.

Aromatic carbon signals experimentally were appeared in the region 126.11-136.63 ppm for phenyl moiety while the chemical shifts of the aromatic carbon atoms theoretically around 126.033-147.51 ppm.

3.5. Optical Study

3.5.1. UV spectra

The experimental and calculated UV–Vis absorption spectra of $(C_8H_{12}N)ClO_4$ were recorded in Fig. 7a and Fig. 7b. A good correlation between the two spectra is observed.

The absorption experimental spectrum exhibits two distinct absorption bands centered at 264 and 281 nm, respectively. The first band observed at 264 nm is attributed to the π–π* transition relating to the aromatic ring of the organic unit. The second band observed at 281 nm is attributed to the n-π * transition of the perchlorate group. The calculated UV–Vis spectrum of the same compound displays also two strong absorption at 218 nm and 241 nm which is attributed to the n-π * and π- π* transitions. Besides, the calculated UV-Vis spectrum is consistent with the experimental one.

In addition, the gap energy which is the energy difference of the two molecular orbitals can be determined from the UV-visible spectrum using the method proposed by Tauc [35] which by simple extrapolation of the affine part of the curve $[\alpha h\nu]^2$ as a function of hν as shown in Fig. 7c.The value of the gap energy is (Eg = 5.43eV). This value is close to the theoretically calculated gap energy. We conclude that the crystal admits a semiconductor property and useful for applications in optoelectronics [36].

3.5.2. Fluorescence properties

The luminescent properties of $(C_8H_{12}N)ClO_4$ was measured in the solid state at room temperature under the excitation of 264 nm. The fluorescence spectra of crystal are given in Fig. S1. It shows two luminescence bands; at 271 nm and 348 nm can be assigned respectively to π*– π transition of aromatic ring of 2-methylbenzylammonium cation and to the n*-π transition of the perchlorate group.

3.6. Frontier molecular orbitals

The Highest Occupied Molecular Orbital (HOMO) and the Lowest Unoccupied Molecular Orbital (LUMO) are the main orbital take part in chemical stability and chemical reactivity of species. The molecular orbital plots of title compound $(C_8H_{12}N)ClO_4$ are shown in Fig. 8, the red and the green colors of the plots correspond to the positive and the negative phase. Orbital analysis revealed that HOMO components are localized on the anionic part while the LUMO components are mainly located on the organic cation.

The energies values of molecular orbitals and their energy gap are used to determine the global reactivity descriptors according to Koopman's theorem [37] such as global softness (S), electron affinity (A), ionization potential (I), electronegativity (χ), chemical hardness (η), electrophilicity index (ω) and chemical potential (μ). All this parameter were calculated at the B3LYP/6-311G(d,p) level and tabulated in **Table 6**.

The calculated energies values of HOMO and LUMO were found to be -7.571 and -1.701 eV, respectively, corresponding to HOMO-LUMO gap of 5.870 eV. Also the energies of HOMO-1 and LUMO+1 are reckoned at -7.598 and -1.289 eV, respectively. The band gap between HOMO-1 and LUMO+1 is observed as 6.309 eV. These results are similar to those observed in other compounds with perchlorate anion [38].

Note that the high value of the gap energy indicates a high kinetic stability and a low chemical reactivity. In addition, it is seen that the negative values of Chemical potential (μ=-4.636eV) shows that the molecule is quite stable.

The smaller value of global hardness (η=2.935eV) designates that the compound has a high polarizability. Moreover, the high ionization potential (I =7.571eV) indicates high reactivity of atom and molecule.

3.7. Quantum theory of atoms in molecules (QTAIMs) analysis

The Bader's theory of Atoms In Molecules (AIM) [39] is useful to investigate bonding nature, energy, and intermolecular interactions. The chemical bond involving in Hydrogen bonding is defined by a bond critical point (BCP) [40]. Fig. 9 discloses the molecular graph which contains the BCPs in $(C_8H_{12}N)ClO_4$ asymmetric unit. It revealed one BCP between non bonded atoms O24–H4, and one ring critical point (RCP). The presence of the BCP justifies the existence of the N-H…O hydrogen bond.

The Topological parameters such as the electron density (ρ), Laplacian of electron density ($\nabla^2\rho$) (is the sum of three eigenvalues of the Hessian matrix (λ1, λ2, λ3)), eigenvalues of Hessian (λ1, λ2, λ3), Hamilton kinetic energy (H(r)= G(r)+V(r), electron kinetic (G(r)) , potential (V(r)) energy densities at bond critical points (BCPs); Bond ellipticity ε (ε= (λ1/λ2-1), where λ1 and λ2 are negative eigenvalues of Hessian of the charge density at BCP (λ1< λ2 < 0 < λ3)) calculated with Multiwfn program [41] provide information about the strength and characteristics of the chemical bonds and more particularly the hydrogen bonds.

According to Rozas et al. [42] the hydrogen bond interactions may be classified as follows: Weak hydrogen bonds if $\nabla^2\rho$(r BCP) > 0 and H(r BCP) > 0, moderate hydrogen bonds if $\nabla^2\rho$(r BCP) > 0 and H(r BCP) < 0 and Strong or very strong hydrogen bonds if $\nabla^2\rho$(r BCP) < 0 and H(r BCP) < 0. **Table 7** regroups all the topological parameters calculated at the BCP. As shown in this table the value of ($\nabla^2\rho(\rho)$) is positive $1.748532675.10^{-2}$ a.u, and the energy density is also positive $4.045385929.10^{-3}$ indicates that the interaction of the hydrogen bond is weak. We can see also the low value of density and positive values of its Laplacian ($\nabla^2\rho$(O24 –H4)) at the BCP indicate the presence of significant hydrogen bond interactions.

3.8. Reduced density gradient (RDG) analysis

The fundamental objective of this analysis is to study the non-covalent interactions the different entities in areas or regions of low density. RDG analysis shows color codes that reveals graphical visualization of weak interactions such as repulsive interactions, van der Waals interactions and hydrogen bonds. Fig. 10 presents the highlights of the RDG function isosurface with sign(λ_2)ρ coloring scheme for $(C_8H_{12}N)ClO_4$. Generally we can determine the types of interactions by examining the sign of the second eigenvalue λ_2, which is a good

indicator of the stabilizing or destabilizing character of an intermolecular interaction (Fig. S2). The positive ($\lambda_2 > 0$) and negative ($\lambda_2 < 0$) signs correspond respectively to the repulsive and attractive regions. From the sign $(\lambda_2)*\rho$, it is possible to evaluate the bond strength. The blue-colored peaks with low RDG on the negative x-axis ($\lambda_2 < 0$) refer to attractive interactions and in particular to strong hydrogen bonds N –H… O and C-H…O. The red peaks in the ring center and around methyl and methylene with high RDG values ($\lambda_2 > 0$) correspond to destabilizing repulsive interactions which show a strong steric effect and in particular to C-H … π interactions similar to those found in benzene [43,44] where a large RDG surface appears that encompasses the whole region of the aromatic ring.

3.9. Molecular electrostatic potential (MEP)

The electrostatic potential map of $(C_8H_{12}N)ClO_4$ shown in Fig. S3 illustrates the charge distribution of the molecule in three dimensions. In fact, this map is used to determine the electrophilic and nucleophilic sites as well as the interactions of the hydrogen bond [45-47]. Additionally, the mapped surface of $(C_8H_{12}N)ClO_4$ exhibits regions of positive, negative and neutral electrostatic potential in terms of color gradation where blue color indicates strong attraction (electrophilic attack) while red shows a region of strong repulsion (nucleophilic attack) and green indicates the neutral zone. It is worth noticing that the electrostatic potential increases in the following order Red <Orange <Yellow <Green <Blue [48]. In this context, the red surfaces of the negative potentials shown in Fig. S3 are associated with the free doublets of the oxygen atoms come from the perchlorate groups accepting the H^+ proton. Moreover, the blue areas of the positive potentials are attributed to the ammonium group of the 2-methylbenzylammonium cation. Also the nucleophilic site (excess electrons) is observed with a dark red color at the level of oxygen atoms bound to ClO_4 of anions and the electrophilic site (deficient in electrons) is observed with a dark blue color at the level of the hydrogen atoms for ammoniums groups. Hence oxygen is expected to be the most reactive site for electrophilic attack and the hydrogen atom will be that of nucleophilic attack in molecule.

3.10. Antibacterial activity

2-methylbenzylammonium perchlorate were screened in vitro as potent antibacterial agents against four referential strains: two pathogenic gram-negative strains named *Escherichia coli* ATCC 8739 G(-), *Salmonella typhimurium* ATCC 14028 G(-) gram and two

pathogenic gram-positive strains named *Staphylococus aureus* ATCC 6538 G(+), *Enterococcus feacium* ATCC 19434 G(+) using disc diffusion method.

The antimicrobial activity against the microorganisms used in the present study was assessed qualitatively and quantitatively in depending on the presence or absence of zones inhibition and the diameter of the zone through compared to ampicillin used like antibiotic drug and reference. The results of measurements of inhibition diameters are given in the **Table 8** and displayed in Fig. S4.

The results reveal that the highest levels marked activity was recorded by 2-methylbenzylammonium perchlorate against Gram (-) *Escherichia coli* ATCC 8739 and *Salmonella typhimurium* ATCC 14028 with a diameter inhibition of 8.75mm and 9.5mm, respectively. The two bacteria *Staphylococus aureus* ATCC 6538 G(+) and *Enterococcus feacium* ATCC 19434 G(+) show less antimicrobial activity. Hence, Gram(-) bacteria were more sensitive to this extract than Gram(+). It is worth noting that $(C_8H_{12}N)ClO_4$ is active against the four microorganisms probably by inhibition of multiplication of these microbes by blocking them using hydrogen bonds and van der Waals interactions [49].

Evaluation of the anti-Candida activity of compound $(C_8H_{12}N)ClO_4$ was performed on a clinical strain called *Candida albicans* ATCC 10231. **Table 8** and Fig. S4 summarize the results of the antifungal activity against *C. albicans* of studied compound by measuring the diameters of inhibitions by comparing with Nystatin (100 µg) of diameter 19.83mm as reference. For antifungal activity, the result was shown an inhibition diameter of value 8.25 mm. Therefore, the synthesized compound manifested an antifungal effect by annihilation of the yeast development route.

Conclusion

The molecular structure of the novel compound was confirmed by single crystal X-ray structural analysis. The crystal structure of is stabilized by N-H…O, and C-H…O hydrogen bonds. Moreover, 2-methylbenzylammonium shows a C-H…π interaction adding extra stability to the three-dimensional architecture. Hirshfeld surface analysis proved that the structure was stabilized by hydrogen bonding. The optimized geometric parameters (bond lengths and bond angles) were theoretically determined and compared with the experimental results. Optical properties show an important Gap energy confirming the semiconductor behavior. The ^{13}C NMR chemical shift has well coherent with experimental and theoretical result. The non-covalent interactions were studied through AIM and RDG analysis. The HOMO-LUMO gap is 5.870 eV for compound which indicates the chemical stability. Finally,

the material show potent antimicrobial efficacy against two pathogenic microbes which can make them applicable as antibacterial agents.

Acknowledgements

We are grateful to the Tunisian Ministry of Higher Education Scientific Research for the provided support.

Supplementary Information: Figs. S1-S4.

Crystallographic data for the structural analysis have been deposited at the Cambridge Crystallographic Data centre, CCDC No 2087625. These data can be obtained free of charge via https: //www.ccdc.cam.ac.uk/conts /re- tri eving.html, or from the CCDC, 12 Union Road, Cambridge, CB2 1EZ, UK: fax: (+ 44) 01223–336–033; e-mail: deposit@ccdc.cam.ac.

References

[1] L.M. Novena, S.S. Kumar, S. Athimoolam, Improved solubility and bioactivity of theophylline (abronchodilator drug) through its new nitrate salt analyzed by experimental and theoretical approaches, J. Mol. Struct. 1116 (2016) 45-55.

[2] A. Müller, F. Peters, M.T. Pope, D. Gatteschi, Polyoxometalates: very large clusters-nanoscalemagnets, Chem. Rev. 98 (1998) 239-272.

[3] P.V. Braun, P. Osenar, V. Tohver, S.B. Kennedy, S.I. Stupp, Nanostructure templating in inorganic solids with organic lyotropic liquid crystals, J. Am. Chem. Soc. 121 (1999) 7302-7309.

[4] M.-C. Daniel, D. Astruc, Gold nanoparticles: assembly, supramolecular chemistry, quantum-size-related properties, and applications toward biology, catalysis, and nanotechnology, Chem. Rev. 104 (2004) 293-346.

[5] P. Englebienne, A.V. Hoonacker, Gold-conductive polymer nanoparticles: a hybrid material with enhanced photonic reactivity to environmental stimuli, J. Colloid Interface Sci. 292 (2) (2005) 445e454.

[6] A. Müller, H. Reuter, S. Dillinger, Supramolecular inorganic chemistry: small guests in small and large hosts, Angew. Chem., Int. Ed. Engl. 34 (1995)2328-2361.

[7] Y. Li , Y. Yu , L. Wu , J. Zhi ,Processable polyaniline/titania nanocomposites with good photocatalytic and conductivity properties prepared via peroxotitanium complex catalyzed emulsion polymerization approach, Appl. Surf. Sci. 273 (2013) 135–143.

[8] a) R. Salmasi, A. Salimi, M. Gholizadeh, M. Rahmani, J.C. Garrison, Symmetric quaternary phosphonium cation and perchlorate/chlorate anions: crystal structure, Database study and Hirshfeld surface analysis, J. Mol. Struct. 1179 (2019) 549-557.

b) Y. Shang, Z. Wang, X. Xu, B. Gao, Z. Ren, Bio-reduction of free and laden perchlorate by the pure and mixed perchlorate reducing bacteria: considering the pH and coexisting nitrate, Chemosphere 205 (2018) 475-483;

c) R. Lancaster, Fireworks: Principles and Practice, Chemical Publishing Co., Inc., New York, 1992.

[9] L. Chen, H. Chen, M. Shen, Z. Zhou, A. Ma, Analysis of perchlorate in milk powder and milk by hydrophilic interaction chromatography combined with tandem mass spectrometry, J. Agric. Food Chem. 58 (2010) 3736–3740.

[10] L. Yu , J.E. Cañas , G.P. Cobb , W.A. Jackson , T.A. Anderson , Ecotoxicol. Environ. Saf. 58 (2004) 44–49 .

[11] W.A. Jackson , P. Joseph , P. Laxman , P.N.Smith K.Tan , T.A.Anderson L.Yu , J. Agric. FoodChem. 53 (2005) 369–373.

[12] A. Srinivasan, T. Viraraghavan, Perchlorate: Health Effects and Technologies for Its Removal from Water Resources, Int. J. Environ. Res. Public Health 6 (2009) 1418-
1442.

[13] R. Srinivasan, G. Sorial, Treatment of perchlorate in drinking water: A critical review, Sep. Purif. Technol. 69 (2009) 7–21.

[14] E. T. Urbansky, Perchlorate Chemistry: Implications for Analysis and Remediation, Biorem. J. 2 (1998) 81–95.

[15] Bruker, APEX2, SAINT and SADABS, Bruker AXS Inc., Madison,Wisconsin, USA,2006.

[16] G.M. Sheldrick, Crystal structure refinement with SHELXL, Acta Crystallogr. C71 (2015) 3-8.

[17] L.J. Farrugia, WinGX and ORTEP for windows: an update, J. Appl. Crystallogr. 45 (2012) 849-854.

[18] R. Dennington, T. Keith, J. Millam, GaussView, Version 5, Semichem. Inc, Shawnee Mission, KS, 2009.

[19] M.J. Frisch, G.W. Trucks, H.B. Schlegel, G.E. Scuseria, M.A. Robb,J.R. Cheeseman, G. Scalmani, V. Barone, B. Mennucci, G.A. Petersson,H. Nakatsuji, M. Caricato, X. Li, H.P. Hratchian, A.F. Izmaylov, J. Bloino,G. Zheng, J.L. Sonnenberg, M. Hada, M. Ehara, K. Toyota, R. Fukuda,J. Hasegawa, M. Ishida, T. Nakajima, Y. Honda, O. Kitao, H. Nakai, T.

Vreven,J.A. Montgomery Jr., J.E. Peralta, F. Ogliaro, M. Bearpark, J.J. Heyd, E. Brothers,K.N. Kudin, V.N. Staroverov, R. Kobayashi, J. Normand, K. Raghavachari, A. Rendell, J.C. Burant, S.S. Iyengar, J. Tomasi, M. Cossi, N. Rega, J.M. Millam, M. Klene, J.E. Knox, J.B. Cross, V. Bakken, C. Adamo, J. Jaramillo, R. Gomperts, R.E. Stratmann, O. Yazyev, A.J. Austin, R. Cammi, C. Pomelli, J.W. Ochterski, R.L. Martin, K. Morokuma, V.G. Zakrzewski, G.A. Voth, P. Salvador, J.J. Dannenberg, S. Dapprich, A.D. Daniels, O. Farkas, J.B. Foresman, J.V. Ortiz, J. Cioslowski, D.J. Fox, GAUSSIAN 09, Revision E.01, Gaussian, Inc., Wallingford CT, 2009.

[20] A.D. Becke, Becke's three parameter hybrid method using the LYP correlation functional, J. Chem. Phys. 98 (1993) 5648-5652.

[21] C. Lee, W. Yang, R.G. Parr, Development of the Colle-Salvetti correlation energy formula into a functional of the electron density, Phys. Rev. 37 (1988) 785-789.

[22] S.K. Wolff, D.J. Grimwood, J.J. McKinnon, D. Jayatilaka, M.A. Spackamn, CrystalExplorer 3.1, University of Westren Australia, Perth, 2013.

[23] T. Lu, F. Chen, Multiwfn: A multifunctional wavefunction analyzer, J. Comput. Chem. 33 (2012) 580-592.

[24] W. Humphrey, A. Dalke, K. Schulten, VMD: Visual molecular dynamics, J. Mol. Graph. 14 (1996) 33-38.

[25] G. Tadesse, E. Ephraim, M. Ashenafi, Assessment of the antimicrobial activity of lactic acid bacteria isolated from Borde and Shamita, traditional Ethiopian fermented beverages, on some foodborne pathogens and effect of growth medium on the inhibitory activity, Int. J. Food Saf. 5 (2005) 13-20.

[26] O.Y. Celikatas, E. Bendir, F.V. Sukan, In vitro antioxidant activities of Rosmarinus officinalis extracts treated with supercritical carbon dioxide, Food Chem. 101 (2007) 1457-1464.

[27] G. Sacchetti, S. Maietti, M. Muzzoli, M. Scaglianti, S. Manfredini, M. Radice, R. Bruni, Comparative evaluation of 11 essential oils of different origin as functional antioxidants, antiradicals and antimicrobials in foods, Food Chem. 91 (2005) 621-632

[28] A. Guesmi, T. Roisnel, H. Marouani, Featuring non-covalent interactions in m-xylylenediaminium bis(perchlorate) monohydrate: Synthesis, characterization and Hirshfeld surface analysis, J. Mol. Struct. 1194 (2019) 66-72.

[29] C. Ben Mleh, T. Roisnel, H. Marouani, Synthesis and crystal structure of a new 2,6-dimethylpiperazine-1,4-diium perchlorate monohydrate: $[C_6H_{16}N_2](ClO_4)_2.H_2O$, Crystallogr. Rep. 62 (2) (2017) 246-248.

[30] W.H. Baur, Acta Crystallogr. B30 (1974) 1191-1195.

[31] S. Gatfaoui, H.Marouani, M. Rzaigui, 4-Methylbenzylammonium nitrate, Acta Cryst. E69 (2013) o1453.

[32] H. Dhaouadi, H. Marouani, M. Rzaigui, A. Madani. Synthesis, Crystal Structure, and Conductivity Investigation of a New Monophosphate: $(2\text{-}CH_3OC_6H_4CH_2NH_3)H_2PO_4$, Phosphorus Sulfur Silicon Relat. Elem. 181:8(2006) 1801 – 1814.

[33] C. Jelsch, K. Ejsmont, L. Huder, The enrichment ratio of atomic contacts in crystals, an indicator derived from the Hirshfeld surface analysis, IUCrJ 1 (2014) 119–128.

[34] K. Wolinski, J.F. Hinton, P. Pulay, Efficient implementation of the gauge independent atomic orbital method for NMR chemical shift calculations, J. Am. Chem. Soc. 112 (1990) 8251-8260.

[35] J. Tauc, Optical properties and electronic structure of amorphous Ge and Si, Mater. Res. Bull. 3 (1968) 37–46.

[36] B.K. Periasamy, R.S. Jebas, B. Thailampillai, Synthesis and spectral studies of 2-aminopyridinium *para*-nitrobenzoate: A novel optoelectronic crystal, Mat. Lett. 61 (2007) 1489-1491.

[37] R. G. Parr, W. Yang, Density Functional Theory of Atoms and Molecules, Oxford University Press, New York, 1989.

[38] C. Daghar, N. Issaoui, T. Roisnel, V. Dorcet, H. Marouani, Empirical and computational studies on newly synthesis cyclohexylammonium perchlorate, J. Mol. Struct. 1230 (2021) 129820.

[39] R.F.W. Bader, Atoms in Molecules, A Quantum Theory, Oxford University Press, Oxford, 1990 ISBN

[40 I. Jomaa, N. Issaoui, T. Roisnel, H. Marouani, Insight into non-covalent interactions in a tetrachlorocadmate salt with promising NLO properties: Experimental and computational analysis, J. Mol. Struct. 1242 (2021) 130730.

[41] T. Lu , F. Chen , Multiwfn: a multifunctional wavefunction analyzer, J. Comput. Chem. 33 (2012) 580–592 .

[42] I. Rozas, I. Alkorta, J. Elguero, Behavior of Ylides Containing N, O, and C Atoms as Hydrogen Bond Acceptors, J. Am. Chem. Soc. 122 (2000) 11154–11161.

[43] G. Saleh, C. Gatti, L. Lo Presti, J. Contreras-Garcia, Revealing non-covalent interactions in molecular crystal through their experimental electron densities, Chem. Eur J. 18 (2012) 15523-15536.

[44] I. Jomaa, O. Noureddine, S. Gatfaoui, N. Issaoui, T. Roisnel, H. Marouani. Experimental, computational, and in silico analysis of $(C_8H_{14}N_2)_2[CdCl_6]$ compound, J. Mol. Struct, 1213 (2020) 128186.

[45] A.E. Reed, F. Weinhold, Natural localized molecular orbitals, J. Chem. Phys. 83 (1985) 1736–1740.

[46] B. Kosar, C. Albayrak, Spectroscopic investigations and quantum chemical computational study of (*E*)-4-methoxy-2-[(p-tolylimino)methyl]phenol, Spectrochim. Acta A78 (2011) 160–167.

[47] M. Tahenti, S.Gatfaoui, N. Issaoui, T. Roisnel, H. Marouani, A tetrachlorocobaltate(II) salt with 2-amino-5-picolinium: Synthesis, theoretical and experimental characterization, J. Mol. Struct, 1207 (2020) 127781.

[48] V. Balachandran, A. Lakshmi, A. Janaki, Conformational stability, vibrational spectral studies, HOMO-LUMO and NBO analyses of 2-hydroxy-4-methyl-3-nitropyridine and 2-hydroxy-4-methyl-5-nitropyridine based on density functional theory, J. Mol. Struct. 1013 (2012) 75–85.

[49] S. Trabelsi, N. Issaoui, S.A. Brandán, F. Bardak, T. Roisnel, A. Atac, H. Marouani, Synthesis and physic-chemical properties of a novel chromate compound with potential biological applications, bis(2-phenylethylammonium) chromate(VI), J. Mol. Struct. 1185 (2019) 168–182.

Figure captions

Fig. 1. ORTEP drawing of $(C_8H_{12}N)ClO_4$ with atoms-labeling scheme. Displacement ellipsoids are drawn at the 30% probability level. Hydrogen bonds are denoted as dashed lines (a) and the optimized molecular structure (b).

Fig. 2. Projection of the $(C_8H_{12}N)ClO_4$ structure along the crystallographic b-axis (a) (Red dashed lines indicate Hydrogen bonds) and along the a-axis (b) (Green dashed lines indicate C-H…π interactions. Hydrogen bond graphs in $(C_8H_{12}N)ClO_4$ (c).

Fig. 3. A view of Hirshfeld surface mapped with d_{norm} [-0.562 - 1.192] (a), shape index [-1 – 1] (b) and curvedness [-4 - 4] (c) for $(C_8H_{12}N)ClO_4$.

Fig. 4. Two-dimensional fingerprint plots of $(C_8H_{12}N)ClO_4$.

Fig. 5. The experimental and theoretical infrared spectra for $(C_8H_{12}N)ClO_4$.

Fig. 6. The experimental ^{13}C NMR spectrum of $(C_8H_{12}N)ClO_4$.

Fig. 7. The experimental (a) and calculated (b) UV-Vis spectra of 2-methylbenzylammonium perchlorate. The energy gap of the title compound (c).

Fig. 8. Frontier molecular orbitals of $(C_8H_{12}N)ClO_4$.

Fig. 9. Graphical representations of the AIM analysis of $(C_8H_{12}N)ClO_4$.

Fig. 10. RDG function isosurface with sign(λ_2)ρ coloring scheme for($C_8H_{12}N)ClO_4$.

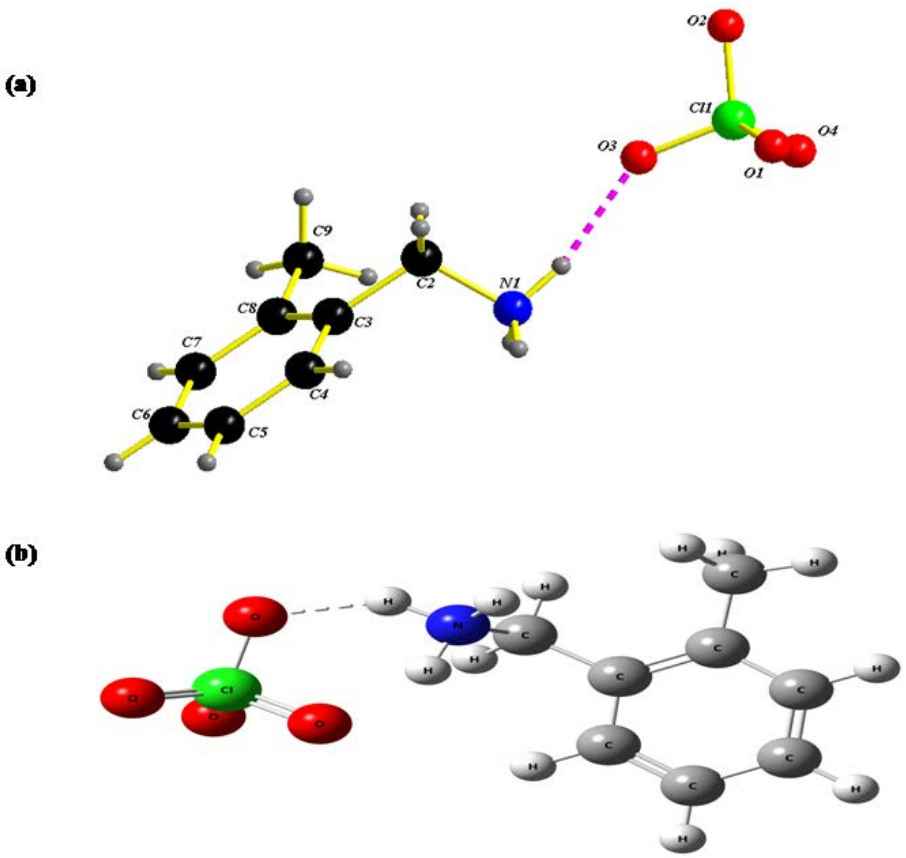

Fig.1. ORTEP drawing of $(C_8H_{12}N)ClO_4$ with atoms-labeling scheme. Displacement ellipsoids are drawn at the 30% probability level. Hydrogen bonds are denoted as dashed lines (a) and the optimized molecular structure (b).

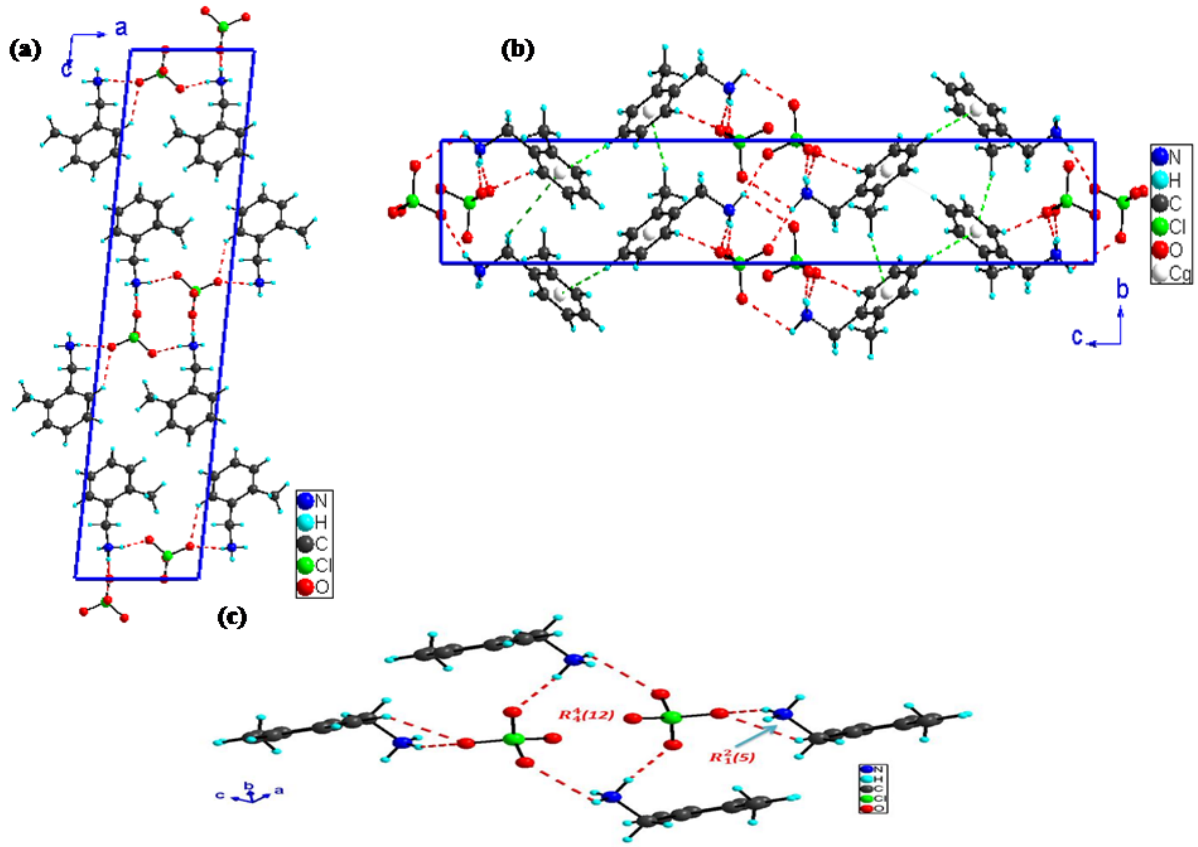

Fig.2. Projection of the $(C_8H_{12}N)ClO_4$ structure along the crystallographic b-axis (a) (red dashed lines indicate Hydrogen bonds) and along the a-axis (b) (Green dashed green lines indicate C-H…π interactions)**.** Hydrogen bond graphs in $(C_8H_{12}N)ClO_4$ (c).

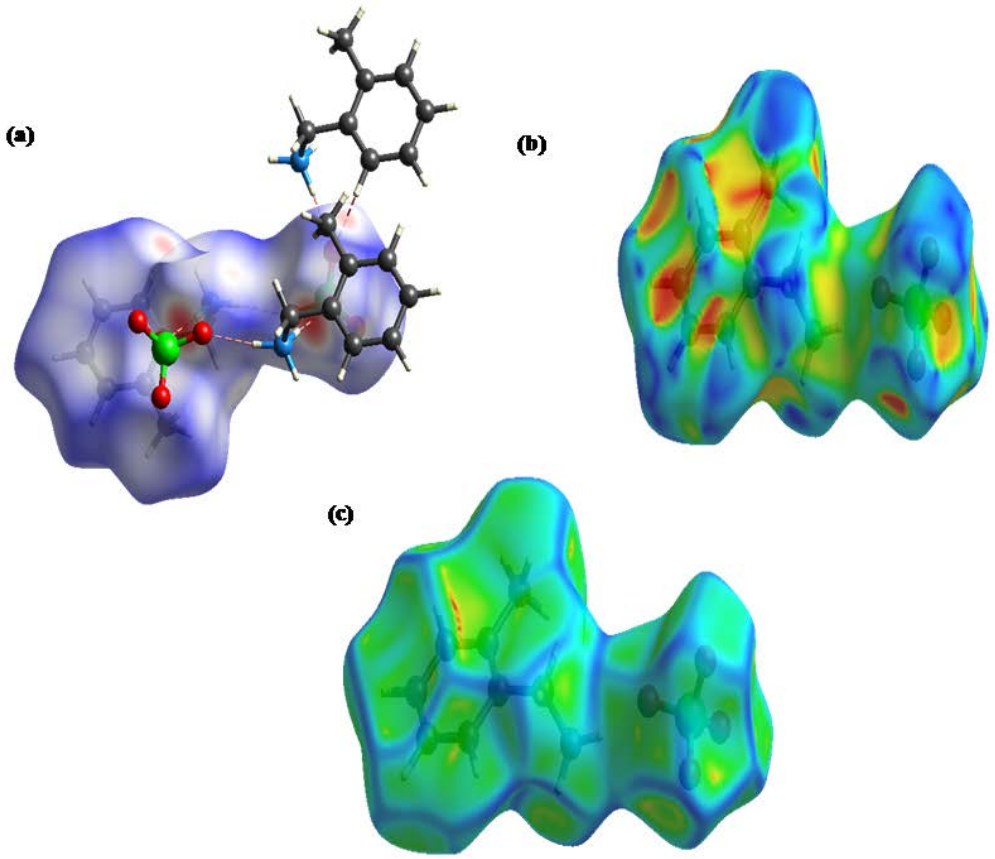

Fig.3. A view of Hirshfeld surface mapped with d_{norm} [-0.562 - 1.192] (a), shape index [-1 – 1] (b) and curvedness [-4 - 4] (c) for $(C_8H_{12}N)ClO_4$.

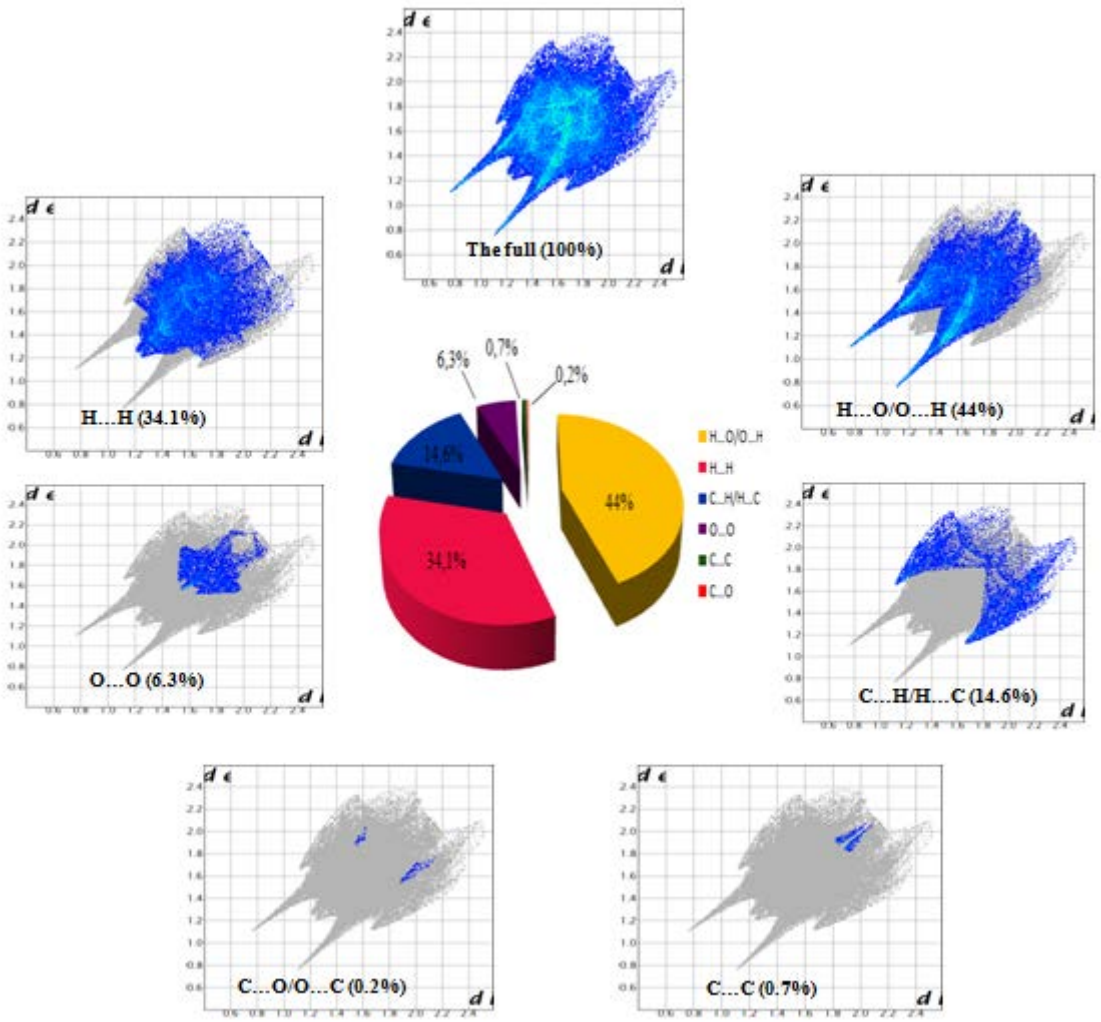

Fig.4. Two-dimensional fingerprint plots of $(C_8H_{12}N)ClO_4$.

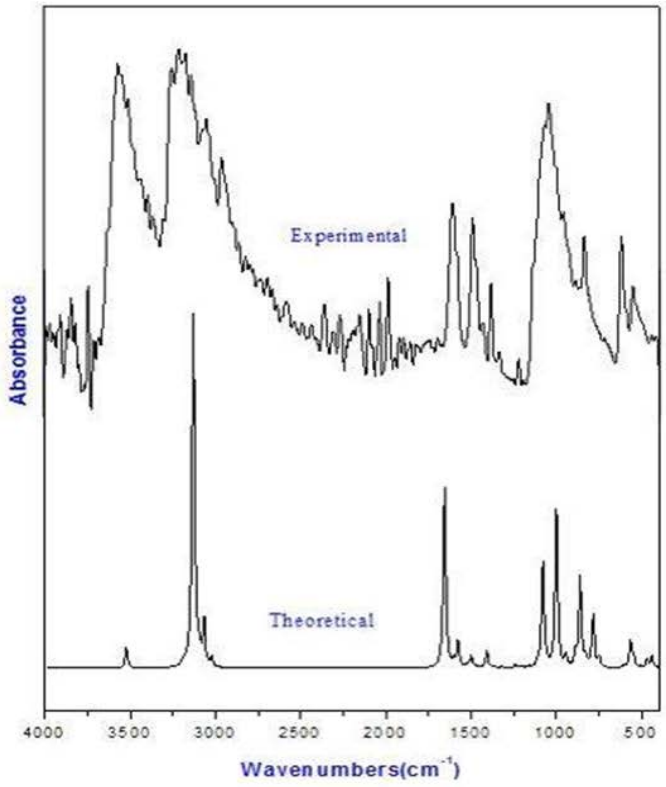

Fig.5. The experimental and theoretical infrared spectra for $(C_8H_{12}N)ClO_4$.

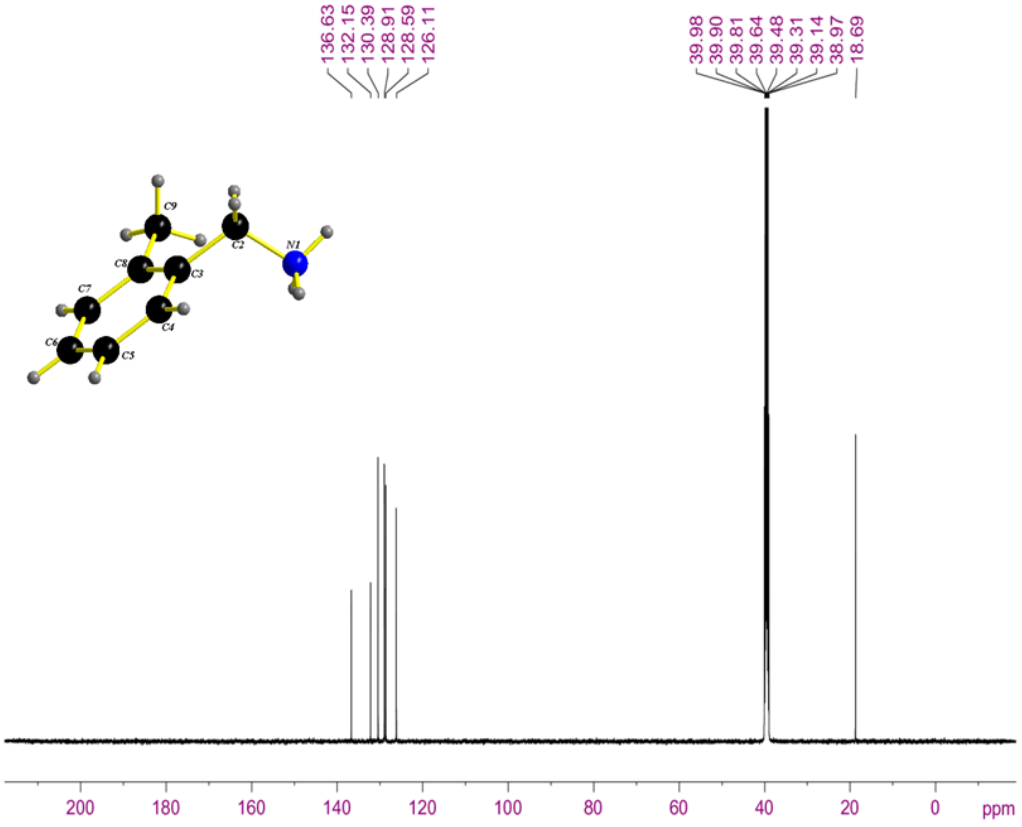

Fig.6. The experimental ^{13}C NMR spectrum of $(C_8H_{12}N)ClO_4$.

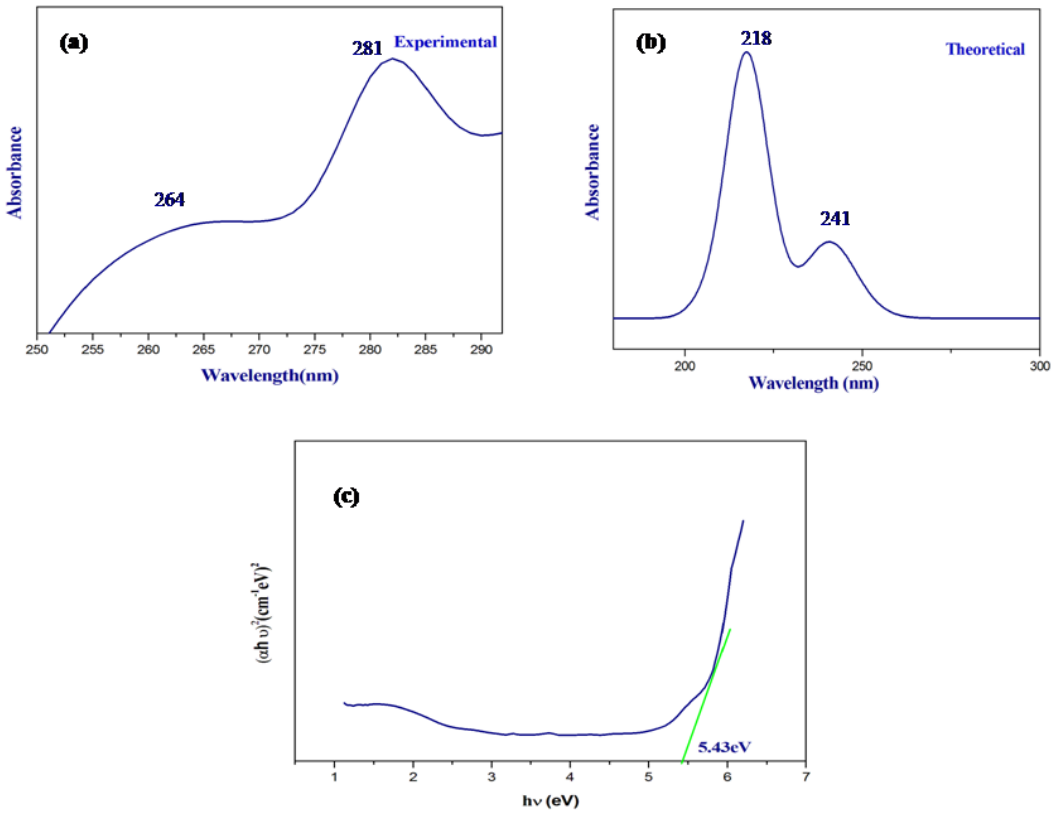

Fig.7. The experimental (a) and calculated (b) UV-Vis spectra of 2-methylbenzylammonium perchlorate. The energy gap of the title compound (c).

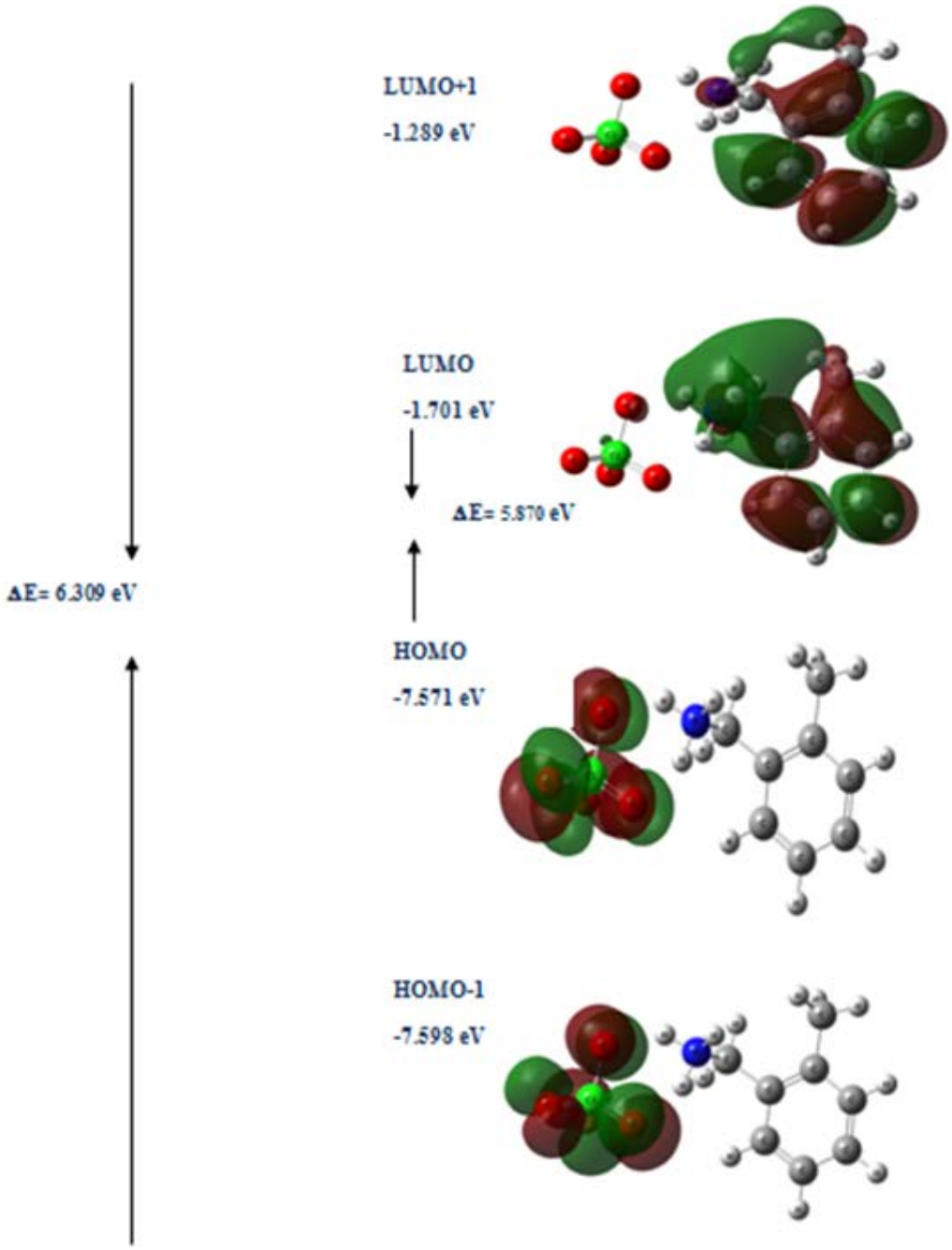

Fig. 8. Frontier molecular orbitals of $(C_8H_{12}N)ClO_4$.

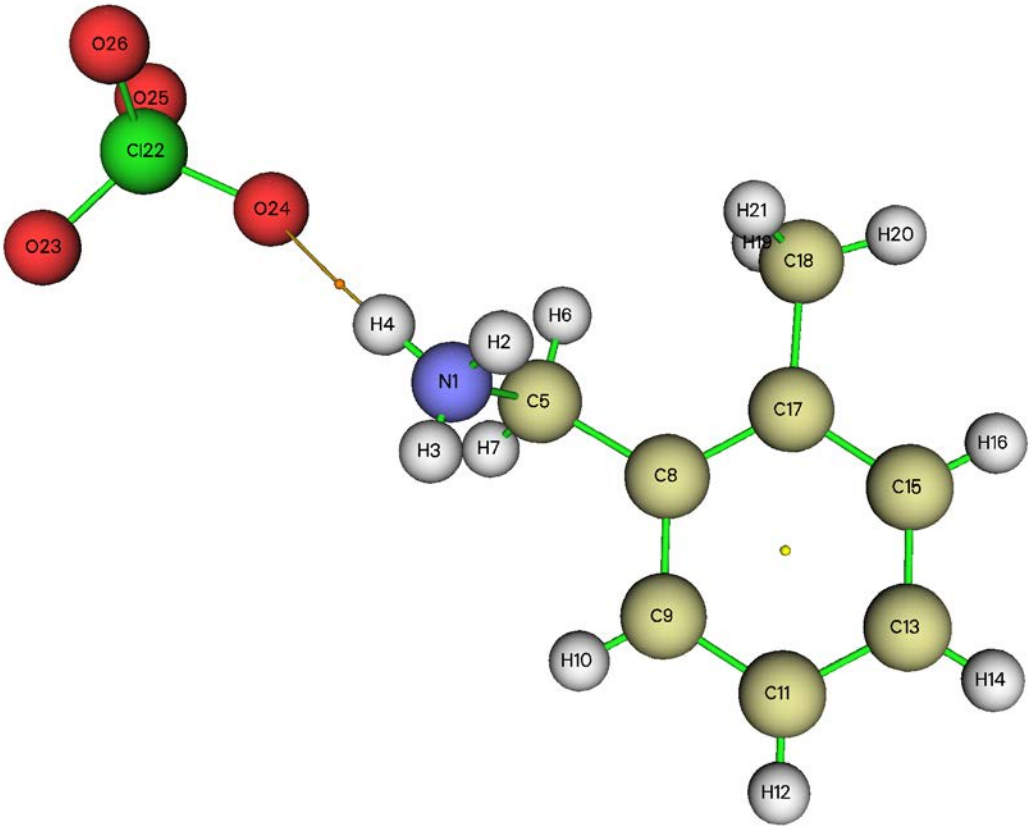

Fig. 9. Graphical representations of the AIM analysis of $(C_8H_{12}N)ClO_4$.

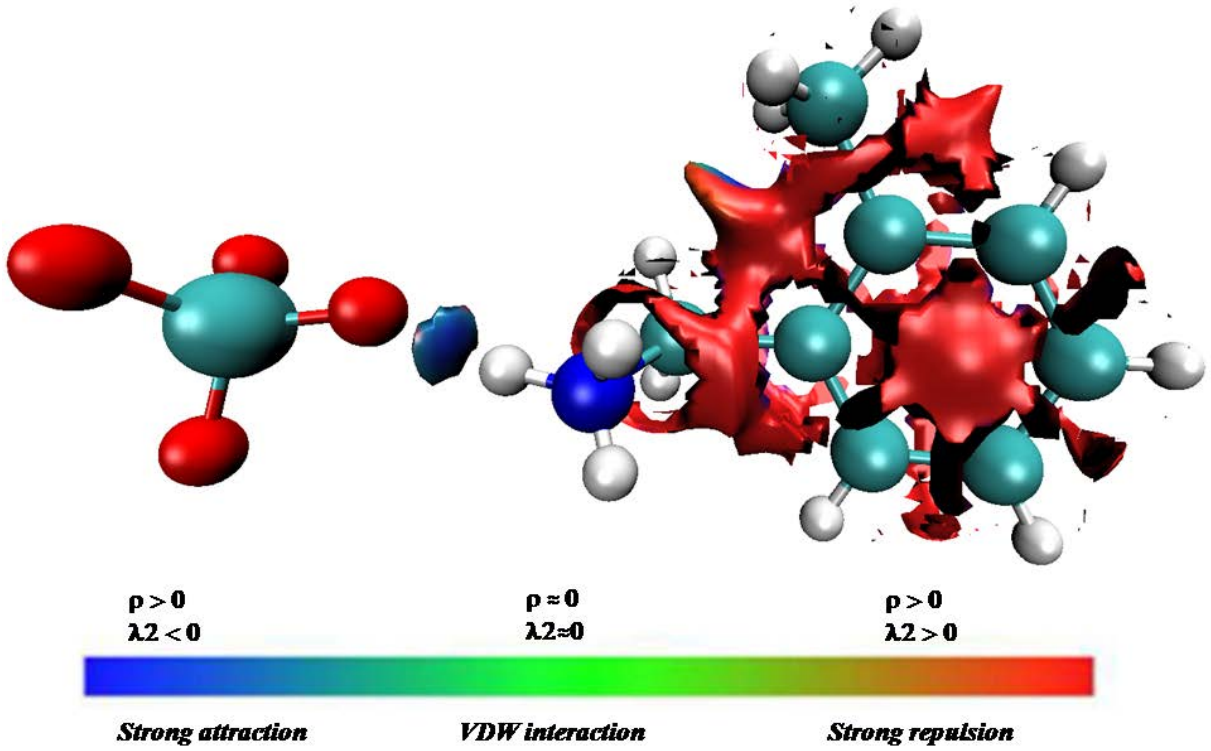

Fig. 10. RDG function isosurface with sign(λ_2)ρ coloring scheme for($C_8H_{12}N)ClO_4$.

Table Captions

Table 1. Crystal data and experimental parameters used for the intensity data collection strategy and results of the structure determination.

Table 2. Theoretical and experimental bond distances (Å) and angles (°) for $(C_8H_{12}N)ClO_4$.

Table 3. Hydrogen-bond geometry of $(C_8H_{12}N)ClO_4$.

Table 4. Enrichment ratio of different inter-contact and percentage of each atom on the surface Hirshfeld in $(C_8H_{12}N)ClO_4$.

Table 5. Theoretically computed and Experimental carbon NMR chemical shifts.

Table 6. Global reactivity descriptors the computed for the title compound.

Table 7. Topological parameters of $(C_8H_{12}N)ClO_4$.

Table 8. Diameters of the Inhibition Zones of different strains for $(C_8H_{12}N)ClO_4$.

Table 1. Crystal data and experimental parameters used for the intensity data collection strategy and final results of the structure determination.

Temperature	150 K
Empirical formula	$C_8H_{12}N(ClO_4)$
Formula weight (g mol^{-1})	221.64
Crystal system	monoclinic
Space group	$P2_1/c$
a	6.8894 (5)Å
b	4.9146 (4) Å
c	29.6565 (18) Å
α	90°
β	96.006 (2) °
γ	90°
Z	4
V	998.62(12) $Å^3$
F(000)	464
μ(Mo Kα)	0.37 mm^{-1}
Index ranges	$-8 \leq h \leq 8$, $-5 \leq k \leq 6$, $-38 \leq l \leq 37$
Reflections collected	7298
Independent reflections	2282
Reflections with $I > 2\sigma(I)$	1948
R_{int}	0.049
Absorption correction: multi-scan	T_{min}= 0.830, T_{max} = 0.914
Refined parameters	103
$R[F^2> 2\sigma(F^2)]$	0.061
$wR(F^2)$	0.152
Goodness of fit	1.05
$\Delta\rho_{max}$ = 0.69 e $Å^{-3}$	$\Delta\rho_{min}$ = −0.81 e $Å^{-3}$

Table 2. Theoretical and experimental bond distances (Å) and angles (°) for $(C_8H_{12}N)ClO_4$.

	Experimental	Theoretically calculated
	Bond-lengths	
N1-C2	1.472(4)	1.509
C2-C3	1.509(3)	1.508
C3-C4	1.390(4)	1.400
C3-C8	1.406(4)	1.409
C4-C5	1,389(4)	1.391
C6-C7	1.372(5)	1.392
C5-C6	1.383(5)	1.393
C7-C8	1.395(4)	1.399
C8-C9	1.504(4)	1.513
Cl22-O23	1.411(3)	1.532
Cl22-O24	1.4270(19)	1.530
Cl22-O25	1.420(3)	1.475
Cl22-O26	1.430(2)	1.468
	Bond-Angles	
N1-C2-C3	112.5(2)	111.38
C5-C8-C9	119.3(3)	118.22
C8-C3-C2	121.1(2)	121.68
C4-C3-C8	119.6(2)	120.10
C5-C4-C3	121.3(3)	120.86
C6-C5-C4	119.1(3)	119.37
C7-C6-C5	119.9(3)	120.00
C6-C7-C8	122.3(3)	121.52
C7-C8-C9	119.8(3)	119.56
O1-Cl1-O2	110.55(18)	106.07
O1-Cl1-O3	110.7(2)	109.12
O1-Cl1-O4	108.00(17)	109.80
O3-Cl1-O2	108.25(15)	109.33
O2-Cl1-O4	110.36(15)	109.77
O3-Cl1-O4	109.01(19)	112.54

Table 3. Hydrogen-bond geometry of $(C_8H_{12}N)ClO_4$.

D—H…A	**D—H (Å)**	**H…A (Å)**	**D···A (Å)**	**D—H...A(°)**
N1—H1*A*···O4^{i}	0.89(4)	1.99(4)	2.876 (4)	168(4)
N1—H1*B*···O1^{ii}	0.77(4)	2.19(4)	2.927 (5)	161(4)
N1—H1*C*···O2	0.92(4)	1.96 (4)	2.861 (3)	168(4)
C2—H2*A*···O4^{iii}	0.99	2.61	3.549 (4)	159
C2—H2*B*···O1^{iv}	0.99	2.64	3.459 (4)	140
C2—H2*A*···Cg^{v}	0.99	3.46	3.997	116
C6—H6···Cg^{vi}	0.95	3.45	4.120	129

Symmetry codes: (i) −*x*+1, −*y*+1, −*z*+1; (ii) −*x*+2, −*y*+1, −*z*+1; (iii) −*x*+1, −*y*+2, −*z*+1; (iv) −*x*+2, −*y*+2, −*z*+1 ; (v) –x+2, y+1/2, -z+3/2; (vi) x, y-1, z.

Cg (gravity center of the ring C3-C4-C5-C6-C7-C8)

Table 4. Enrichment ratio of different inter-contact and percentage of each atom on the surface Hirshfeld in $(C_8H_{12}N)ClO_4$.

Enrichment ratio	**H**	**C**	**O**
H	0.85	1.42	1.22
C		-	
O			-
% Surface	**63.4**	**8.1**	**28.4**

Table 5. Theoretically computed and Experimental carbon NMR chemical shifts.

Atoms	Experimental chemical shift in ppm	Calculated chemical shift in ppm
		TMS B3LYP/6-311+G(2d,p) GIAO (ppm)
C2	38.97	29.386
C3	136.63	147.51
C4	130.39	129.159
C5	128.59	129.159
C6	126.11	126.033
C7	128.91	129.159
C8	132.15	134.868
C9	18.69	29.386

Table 6. Global reactivity descriptors the computed for the title compound.

Parameters (eV)	Values
E_{HOMO}	-7.571
E_{LUMOMO}	-1.701
Energy band gap $\lvert E_{HOMO}–E_{LUMO}\rvert$	5.870
E_{HOMO-1}	-7.598
E_{LUMO+1}	-1.289
Energy band gap $\lvert E_{HOMO-1}–E_{LUMO+1}\rvert$	6.309
Ionization potential ($I = –E_{HOMO}$)	7.571
Electron affinity ($A = –E_{LUMO}$)	1.701
Chemical hardness ($\eta = (I–A)/2$)	2.935
Chemical softness ($S = 1/2\eta$)	0.170
Electronegativity ($\chi = (I+A)/2$)	4.636
Chemical potential ($\mu = –(I+A)/2$)	-4.636
Electrophilicity index $\omega = \mu^2/2\eta$	3.661
Maximum charge transfer index ($\Delta N_{max.} = –\mu/\eta$)	1.579

Table 7. Topological parameters of $(C_8H_{12}N)ClO_4$.

	$H_4 \ldots O_{24}$
Density of all electrons ρ(r) (a.u.)	$1.748532675.10^{-2}$
Lagrangian kinetic energy G(r) (a.u.)	$2.494707156.10^{-2}$
Potential energy density V(r) (a.u.)	$-2.090168563.10^{-2}$
Energy density E(r) or H(r) (a.u.)	$4.045385929.10^{-3}$
Laplacian of electron density $\nabla^2\rho(r)$ (a.u.)	$1.159698300.10^{-1}$
Reduced density gradient (RDG)	$1.612136507.10^{-15}$
Eigen values of Hessian	$1.597841151.10^{-1}$ $-2.104380311.10^{-2}$ $-2.277048204.10^{-2}$
Ellipticity of electron density(ε)	$8.2052.10^{-2}$
Eta index(ζ)	$1.42508.10^{-1}$

Table 8. Diameters of the Inhibition Zones of different strains for $(C_8H_{12}N)ClO_4$.

	Inhibition diameter (mm)	
Name strain\ Disk load (µg)	**Ampicillin/ Nystatin**	**Extract**
	10µg/100µg	2mg
***Escherichia coli* ATCC 8739 G(-)**	11.75±0.3	8.75±0.3
***Salmonella typhimurium* ATCC 14028 G(-)**	13.75±1.0	9.5±0.7
***Staphylococus aureus* ATCC 6538 G(+)**	35.5±0.7	7.75±0.3
***Enterococcus feacium* ATCC 19434 G(+)**	26.5±0.7	7.5±0.0
***Candida albicans* ATCC 10231**	19.83±0.2	8.25±0.3

All data are expressed as the means ± standard deviation (SD) of triplicate measurements.